




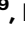



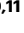






# Optically tunable catalytic cancer therapy using enzyme-like chiral plasmonic nanoparticles

Received: 30 April 2024

Accepted: 28 February 2025

Published online: 15 March 2025

 Check for updates

Haeun Kang <sup>1,19</sup>, Subin Yu <sup>1,2,19</sup>, Ryeong Myeong Kim<sup>3,19</sup>, Youngbi Kim<sup>4</sup>, Sang Chul Shin <sup>5</sup>, Dohyub Jang<sup>6</sup>, Jeong Hyun Han<sup>3</sup>, Sugyeong Hong<sup>7</sup>, Eunice EunKyeong Kim <sup>8</sup>, Sun Hee Kim <sup>7,9</sup>, Dong June Ahn <sup>6,10</sup>, Jeong Woo Han <sup>3</sup> , Sehoon Kim <sup>10,11</sup> , Ki Tae Nam <sup>3</sup> , Luke P. Lee <sup>2,12,13,14</sup>  & Dong Ha Kim <sup>1,15,16,17,18</sup> 

Cascade enzymatic reactions in living organisms are fundamental reaction mechanisms in coordinating various complex biochemical processes such as metabolism, signal transduction, and gene regulation. Many studies have attempted to mimic cascade reactions using nanoparticles with enzyme-like activity; however, precisely tuning each reaction within complex networks to enhance the catalytic activity remains challenging. Here, we present enzyme-like chiral plasmonic nanoparticles for optically tunable catalytic cancer therapy. We create chiral plasmonic nanoparticles with glucose oxidase (GOD) and peroxidase (POD) activities, followed by introducing circularly polarized light (CPL). By sequentially activating GOD and POD reactions with right-handed CPL (RC) followed by left-handed CPL (LC), we achieve 1.25- and 1.9-fold enhanced catalytic performance (overall 1.3 times enhancement) compared to non-controlled cascade reactions by creating an optimal acidic environment for the subsequent reaction. Moreover, the D-Au nanoparticle shows a 2-fold higher binding selectivity to D-glucose substrates, attributed to chirality matching. In both cell studies and male mouse models, sequentially irradiated groups (RC followed by LC) exhibit the highest radical generation and the most efficient treatment outcomes compared to the other systems under different irradiation conditions. We believe that our system holds strong potential for medical applications, suggesting a promising platform for catalytic therapy.

Living organisms are incredibly complex, comprising countless interconnected biochemical pathways. Cascade reactions play a pivotal role in managing this complexity by organizing reactions into sequential steps, where the product of one reaction becomes the substrate for the next<sup>1,2</sup>. Each step in a cascade reaction is catalytically driven, often by enzymes, to produce the necessary outcomes for cellular function,

energy production, and response to environmental stimuli<sup>3–5</sup>. This sequential organization ensures that biological processes proceed in a controlled and orderly manner to conduct complex processes with remarkable precision and efficiency.

Given the critical role of cascade reactions in biological systems, there has been a growing interest in mimicking these processes

A full list of affiliations appears at the end of the paper. ✉ e-mail: [jwhan98@snu.ac.kr](mailto:jwhan98@snu.ac.kr); [sehoonkim@kist.re.kr](mailto:sehoonkim@kist.re.kr); [nkitae@snu.ac.kr](mailto:nkitae@snu.ac.kr); [lplee@bwh.harvard.edu](mailto:lplee@bwh.harvard.edu); [dhkim@ewha.ac.kr](mailto:dhkim@ewha.ac.kr)

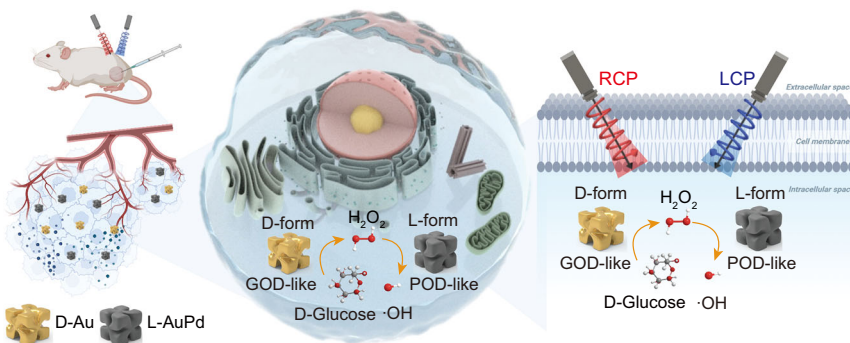
artificially through nanoparticles that exhibit enzyme-like activities<sup>6</sup>. Various nanomaterials, including noble metals<sup>7,8</sup>, transition metals<sup>9–12</sup> and carbon-based materials, have been investigated for their enzyme-mimicking properties such as oxidase-, peroxidase-, and catalase-mimics<sup>13–18</sup>. Notably, noble metals or transition metals such as gold (Au), silver (Ag)<sup>19</sup>, palladium (Pd)<sup>20</sup> and platinum (Pt)<sup>21</sup> have been considered as promising candidates for mediating reactive oxygen species (ROS) generation reactions through their enzyme-mimicking properties<sup>22</sup>. Among them, Pd was known as POD-mimic enzyme-like nanoparticles under acidic conditions<sup>23</sup>, while Au has been recognized as the glucose oxidase (GOD)-mimic, useful for cascade enzymatic activity for catalytic cancer treatment<sup>24</sup>.

Despite the promising potential of nanoparticles in facilitating cascade reactions, their practical application could be improved by substantial challenges. One significant hurdle is the low enzymatic activity of these nanoparticles compared to natural enzymes, coupled with the complexity of achieving precise control of each reaction within the cascade reactions. This discrepancy in efficiency and control limits the effectiveness of such nanoparticle-based systems in replicating the dynamic and finely tuned nature of biological cascade reactions. Furthermore, one of the most characteristic features of natural enzymes compared to enzyme-like nanoparticles is their chiral-dependent substrate specificity and reactivity. Biological substrate molecules have specific handedness, e.g., left-handedness in protein tertiary structures and right-handed sugars<sup>25–28</sup>. Therefore, integration of chirality into the enzyme-like nanoparticles can be the solution to improve the substrate selectivity of the developed nanoparticles. Meanwhile, regarding reactivity, chiral plasmonic nanostructures hold

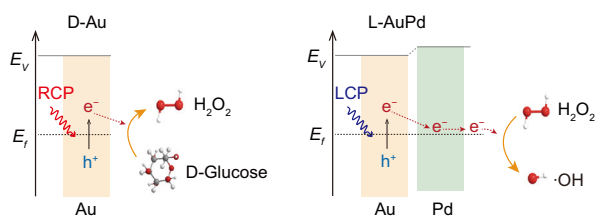
great potential as enzyme-like nanoparticles due to the chiroptical-dependent generation of local electric field and hot charge carriers<sup>29–33</sup>. These features eventually enhance enzymatic activity in a circularly polarized light (CPL)-dependent manner<sup>34</sup>. Incorporating light-matter interaction with the intrinsic handedness of chiral plasmonic nanostructures is expected to improve the overall reactivity of enzyme-like nanoparticles in the biological milieu<sup>35</sup>.

Here, in light of the previously discussed strategic approach, we present advanced chiral hybrid plasmonic nanoparticles that function like enzymes in catalytic cancer therapy, driven by cascade enzymatic actions based on chiroptical properties. (Fig. 1). To control the enzymatic activity of nanoparticles depending on their handedness, we take two prominent strategies based on the characteristic features of our chiral plasmonic enzyme-like nanoparticles: 1) generation of hot carriers dependent on CPL, which can affect enzymatic reactions (Fig. 1d) and 2) enantioselective interaction with substrate D-glucose, the predominant chiral form of glucose in human body (Fig. 1e). Specifically, GOD and POD reactions are sequentially activated using chiral nanoparticles of opposite handedness via stepwise irradiation with RC and LC, respectively. Controlling the sequence of the GOD and POD reactions is crucial for optimizing conditions for individual steps and maximizing the overall reaction, leading to higher yields and fewer unwanted byproducts during cascade reactions. The initially activated GOD reaction provides an acidic environment and substrates for the POD catalyst, enabling more efficient subsequent POD reactions. D-glutathione (GSH)-gold nanoparticles (D-Au) and palladium-coated L-glutathione (GSH)-gold nanoparticles (L-AuPd) are prepared as enzyme-like chiral plasmonic

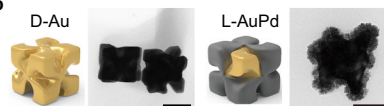
**a** Enantioselective cascade enzymatic activity for chemodynamic cancer therapy



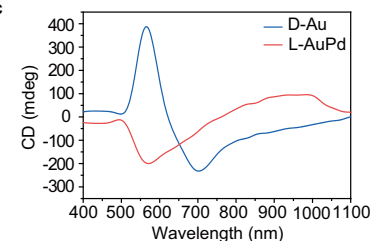
**d** Plasmon-enhanced enzymatic activity



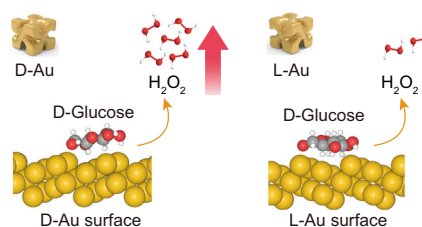
**b**



**c**



**e** Enantioselectively enhanced substrate selectivity



**Fig. 1 | Enantioselective cascade enzymatic activity for catalytic cancer therapy.** **a** Schematic illustration of the cascade enzymatic reaction of chiral plasmonic nanoparticles for catalytic cancer treatment under RC and LC illumination. (created in <https://BioRender.com/w31p822>). D-Au showed enhanced GOD-like activity under RC irradiation to oxidize the D-glu substrate, same handedness with catalyst, to produce the H<sub>2</sub>O<sub>2</sub> and acidic environment, while the L-AuPd effectively decomposed the H<sub>2</sub>O<sub>2</sub> to form hydroxyl radicals via injected hot electrons from chiral plasmonic Au core under the LC illumination, eventually leading to eradication of tumor both in vitro and in vivo. **b** Schematic illustration and TEM image of prepared D-Au and L-AuPd. scale bar = 100 nm. **c** Circular dichroism spectra of D-Au and L-AuPd. **d** Schematic diagram of plasmon-enhanced enzymatic activity of D-Au and L-AuPd under RC and LC, respectively. Under the RC irradiation, chiro-optical

responsive hot charge carriers were generated, and these carriers participated in the oxidation of D-glu to make H<sub>2</sub>O<sub>2</sub>. Under the LC illumination, the L-Au core produced the hot charge carriers, and hot electrons were collected at the Pd shell catalyst site. Collected hot electrons eventually participated in the decomposition of H<sub>2</sub>O<sub>2</sub>, producing cytotoxic hydroxyl radicals. (E<sub>f</sub>: metal Fermi level, E<sub>v</sub>: vacuum level). **e** Schematic diagram of enantioselectively enhanced substrate selectivity according to the chirality of gold nanoparticle. D-glu specifically interacted with the D-Au surface rather than L-Au surface, leading to more adsorption of substrates onto the catalytic site to oxidize the D-glu to H<sub>2</sub>O<sub>2</sub>. These results induced sufficient generation of H<sub>2</sub>O<sub>2</sub> and created the acidic environment for the POD-like activity of L-AuPd. Source data are provided as a Source Data file.

nanoparticles exhibiting mirror symmetry in circular dichroism (CD) spectra (Fig. 1b, c). In detail, D-glucose (D-glu) substrates are enantioselectively bound at the D-Au active site and converted into gluconic acid, simultaneously generating hydrogen peroxide ( $\text{H}_2\text{O}_2$ ) under the handedness-matched light illumination (right-handed CP (RC)). Subsequently, the decomposition of  $\text{H}_2\text{O}_2$  occurs at the L-AuPd active site under left-handed CP (LC), generating cytotoxic hydroxyl radicals ( $\bullet\text{OH}$ ) to eradicate the cancer cells (Fig. 1a). In this work, the underlying rationale of our findings elucidates the significant enhancement in catalytic efficiency achieved through enantioselective substrate selectivity and chiroptically controlled generation of hot carriers through the inherent GOD- and POD-like features of each nanocomponent. In agreement, D-Au responds to the RC illumination, generating hot electrons and holes to participate in the oxidation of D-glu. Meanwhile, hot electrons generated in L-Au by LC illumination are effectively separated by highly electron-withdrawn Pd shells<sup>36</sup>. The resulting localized hot electrons at the Pd site reduce  $\text{H}_2\text{O}_2$  into  $\bullet\text{OH}$ , eventually effectively killing cancer cells via chemo-dynamic therapy. Our work highlights that integrating chiral/chiroptical and plasmonic features into enzyme-like nanoparticles could present the strategy for modulating cascade reactions, ensuring that each reaction occurs under its ideal conditions, thereby maximizing the overall efficiency of the process.

## Results

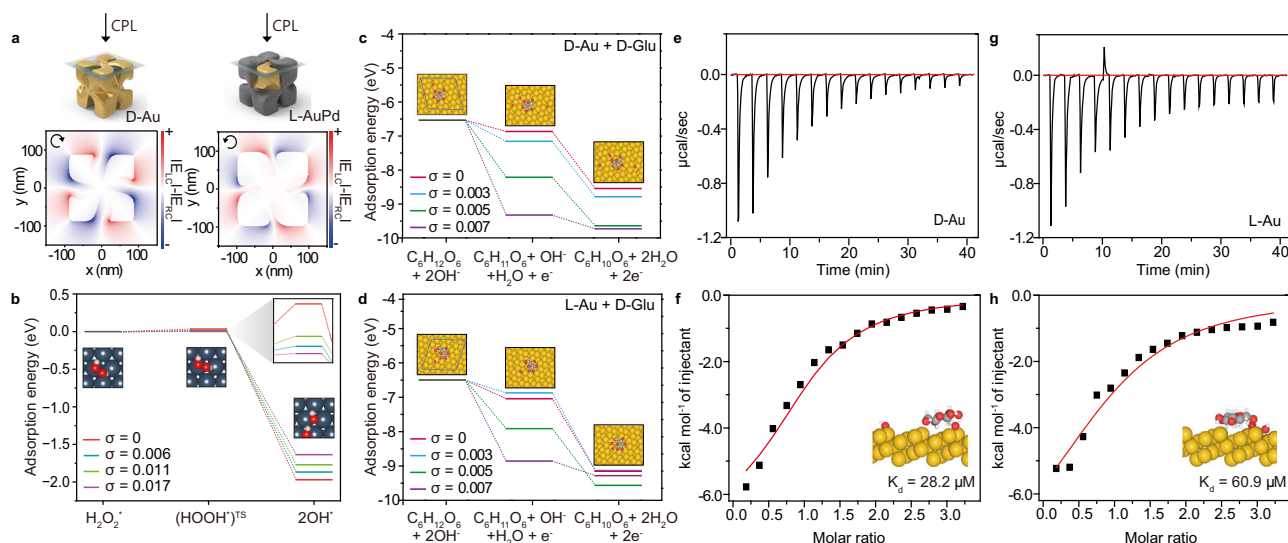
### Characterization of enzyme-like chiral plasmonic nanoparticles

The chiral L-/D-Au were prepared followed by seed-mediated method with the introduction of L-/D-GSH ligand during the growth process as referred to previous literature<sup>32,33,37</sup>. The morphological characterization was proceeded by measuring transmission electron microscopy (TEM) images (Supplementary Fig. S1a, c) and scanning electron microscopy (SEM) images (Supplementary Fig. S1b, d). TEM images displayed the cube-like L-/D-Au with surfaces split in opposite directions with an average diameter of ~100 nm. As-prepared D-Au was selected for GOD-mimic enzyme-like nanoparticles, facilitating the enantioselective interaction with the biological D-glu substrate. Following the synthesis of L-Au, a Pd shell was introduced by reducing the Pd precursor in the presence of ascorbic acid (Supplementary Fig. S2a). The successful incorporation of Pd was verified with SEM images (Supplementary Fig. S2b), TEM images (Fig. 1b and Supplementary Fig. S2c), and high-resolution (HR)-TEM images (Supplementary Fig. S2d–f). Compared to the bare L-Au (Supplementary Fig. S1c, d), bumpy structures were observed at the L-AuPd surface, demonstrating the successful deposition of the Pd NP shell on the L-Au surface. The d-spacing of deposited Pd NPs is around 0.23 nm, corresponding to the (111) plane (Supplementary Fig. S2f). Energy dispersive X-ray (EDX) mapping results showcased the homogeneous distribution of the Pd element (red) at the Au surface (yellow), further suggesting the well-prepared L-AuPd for POD-mimic enzyme-like nanoparticles (Supplementary Fig. S3a). X-ray photoelectron spectroscopy (XPS) spectroscopy was surveyed to validate the oxidation state of Pd at the L-Au surface (Supplementary Fig. S3b, c). The binding energy of Pd  $3d_{5/2}$  and  $3d_{3/2}$  was obtained at 334.5 and 339.8 eV, respectively, for metallic Pd, while partially oxidized Pd existed at the Au surface with increased binding energy at 336.5 and 342 eV. Existing Pd (II) ions would be reduced to metallic Pd, serving as a catalytic active site by a localized hot electron from L-Au, which is feasible for POD-like activity under LC irradiation. The optical properties of prepared enzyme-like chiral plasmonic nanoparticles were then assessed (Supplementary Fig. S4). D-Au and L-Au showed mirror symmetry peaks at 610 nm and 800 nm in the circular dichroism (CD) spectra (Supplementary Fig. S4a) and strong localized surface plasmon resonance (LSPR) bands were monitored in the range of visible and near-infrared region as depicted in Uv-vis-NIR spectra (Figure S4c). The g-factor of L-Au at 808 nm is around 0.0329 while the value of D-Au at

808 nm is -0.0302, suggesting similar CPL-responsiveness of D- and L-Au (Supplementary Fig. S4b). These results confirmed the opposite chiroptical properties of D- and L-Au in the range of vis-NIR region. The LSPR peaks, CD peaks, and g-factor of L-AuPd exhibited noticeable red-shift compared to those of L-Au (Supplementary Fig. S4d–f), attributed to changes in the refractive index surrounding L-Au and the large imaginary number of Pd dielectric function. The g-factor of L-AuPd at 808 nm is 0.0281, indicating well-maintained L-AuPd chirality for using L-AuPd as chiroptical-dependent POD-like enzyme-like nanoparticles (Supplementary Fig. S4e). Despite the small g-factors, hot charge carriers generated under the continuous light irradiation can produce steady-state population of ROS. This can induce differences in the number of ROS molecules photogenerated over time, thereby explaining the significant variations in catalytic activity kinetics between the two light polarizations<sup>34</sup>.

### Mechanism of chiral- and chiroptical-dependent enhanced catalytic performance

We then performed the theoretical analysis to investigate the chiroptical-dependent enhancement of catalytic performance in our enzyme-like chiral nanoparticles (Fig. 2). Light-matter interaction of D-Au and L-AuPd were simulated to confirm the chiroptical properties via finite-difference time-domain (FDTD) simulation under the CPL illumination<sup>33</sup> (Fig. 2a). The differences in these fields under the LC and RC excitation illustrated the asymmetric responses of the electric fields. In the case of D-Au, it exhibited the locally enhanced electric field with a right-handed direction under RC. In contrast, the opposite direction of electric field enhancement was observed in L-Au or L-AuPd under LC irradiation (Fig. 2a, Supplementary Fig. S5). These results emphasized the chiroptical responses of both chiral plasmonic nanostructures, which facilitate the generation of hot charge carriers under the corresponding CPL illuminations (RC for D-Au and LC for L-AuPd). We then performed density functional theory (DFT) calculations to verify the impact of hot charge carriers on the catalytic performance of both GOD-mimic D-Au and POD-mimic L-AuPd under CPL illumination<sup>38</sup> (Fig. 2b–d). Firstly, the influence of hot electrons on the catalytic performance of L-AuPd was investigated. As illustrated in Fig. 1d, LC illumination induced the generation of hot electrons at the Au site and generated hot electrons were concentrated at the Pd catalytic site to decompose the  $\text{H}_2\text{O}_2$ . Previous research demonstrated the enrichment of electrons on Pd through hot electron transfer from the Au site, as evidenced by X-ray absorption near-edge structure (XANES) spectroscopy measurements under light illumination<sup>39</sup>. These findings support the hypothesis that hot electrons are transferred from plasmonic Au to Pd. Thus, for L-AuPd, the calculation was carried out by dividing it into the L-Au surface and the Pd surface. Figure 2b shows the adsorption energy of  $\text{H}_2\text{O}_2$  homolytic dissociation on the Pd surface as a function of hot electron level ( $\sigma$ )<sup>40,41</sup>. With increasing the electron density at the Pd site, the adsorption energy of homolytic dissociation ( $\text{HOOH}^*$ )<sup>42</sup> decreased, confirming that the enrichment of electrons at the Pd site facilitates the decomposition of  $\text{H}_2\text{O}_2$ . The impact of hot holes at glucose oxidation reaction was then simulated for both D-Au and L-Au surfaces as a function of hot hole level ( $\sigma$ ), as illustrated in Fig. 2c, d. The reaction mechanism of noble metal-mediated GOD-like activity is the same as that of natural GOD, except for the role of  $\text{OH}^-$ , which is used to abstract the  $\text{H}^+$  from glucose. The  $\text{H}^+$  in glucose ( $\text{C}_6\text{H}_{12}\text{O}_6 + 2\text{OH}^-$ ) is abstracted by the surrounding  $\text{OH}^-$ , forming an intermediate (first step:  $\text{C}_6\text{H}_{11}\text{O}_6 + \text{H}_2\text{O} + \text{e}^-$ ). Then, the direct hydride transfer occurs from the glucose to the Au surface, forming  $\text{C}_6\text{H}_{10}\text{O}_6$  and releasing  $2\text{e}^-$  (second step). Finally, generated electrons reduce the oxygen to produce  $\text{H}_2\text{O}_2$ <sup>42</sup>. Based on the GOD mentioned above reaction pathway, the initial adsorption of D-glu on each of D-Au, achiral Au, and L-Au was simulated by DFT calculations (Supplementary Fig. S6a–c). The initial adsorption energy of  $\text{C}_6\text{H}_{12}\text{O}_6 + 2\text{OH}^-$  on the D-Au (-6.536 eV) surface is lower compared to



**Fig. 2 | Analysis of chiral- and chiroptical-dependent enhanced catalytic performance.** **a** Schematic illustration showing the plane above the nanoparticle surface utilized for simulation under CPL irradiation and simulated electric field differences under LC and RC excitation for D-Au and L-AuPd, respectively. The color scale represents the magnitude of the field difference, with red indicating positive difference and blue indicating negative difference. **b** Adsorption energy for  $\text{H}_2\text{O}_2$  homolytic dissociation on the Pd surface as a function of the electron level ( $\sigma$ ). The adsorption configuration of reaction intermediates is also shown. The navy, red, and white balls represent Pd, O, and H atoms, respectively. Adsorption energy for the D-glucose oxidation on the (c) D-Au surface and (d) L-Au surface as a

function of the hole level ( $\sigma$ ). The adsorption configuration of reaction intermediates is also shown. The yellow, red, gray and white balls represent Au, O, C and H atoms, respectively. Isothermal Titration Calorimetry (ITC) data of the D-glu interaction with (e), (f) D-Au ( $K_d = 28.2 \mu\text{M}$ ,  $N = 1$  (Fix)) and (g), (h) L-Au ( $K_d = 60.9 \mu\text{M}$ ,  $N = 1$  (Fix)).  $K_d$  represents dissociation constant, and  $N$  represents binding stoichiometry. The experimental data are shown as solid squares, and the least squares' best-fit curves derived from a simple one-site binding model (fixed) are shown as red lines. Insets are the side view of D-glu on Au (321) surface. The yellow, red, gray and white balls represent Au, O, C and H atoms, respectively. Source data are provided as a Source Data file.

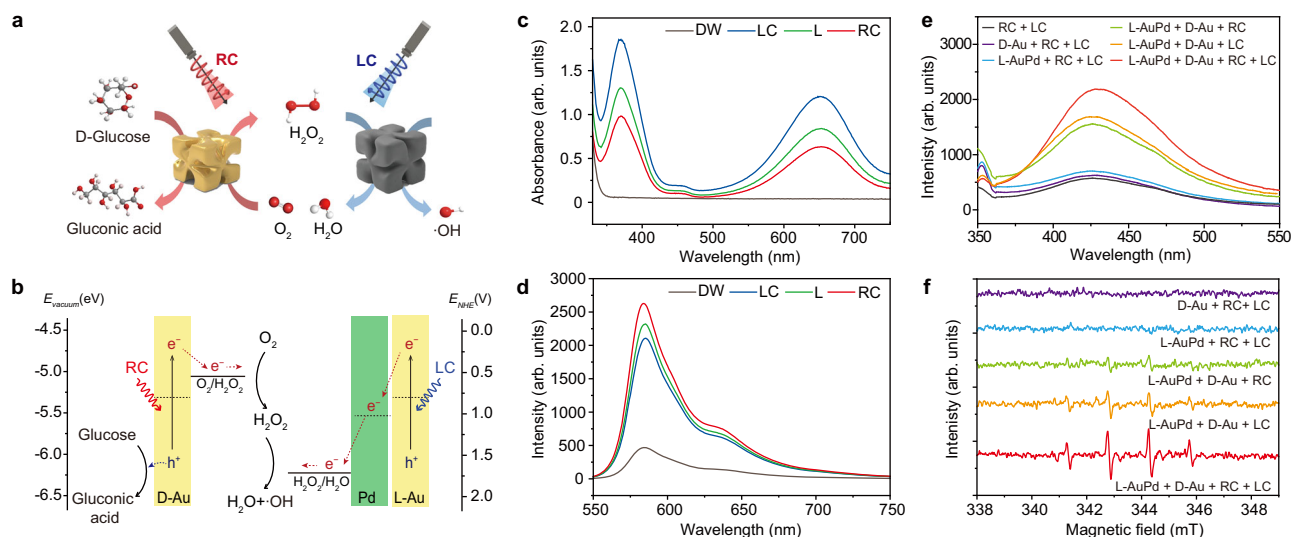
that on the L-Au ( $-6.499 \text{ eV}$ ) and achiral Au ( $-6.410 \text{ eV}$ ) surface, suggesting that the most stable adsorption of D-glu occurred at the D-Au surface. After confirming the initial adsorption of D-glu, we calculated the adsorption energy for each oxidation reaction step of D-glu at both D-Au and L-Au with increasing the hole level at the Au surface. In the case of D-Au, by increasing the hole level at each step, the adsorption energy was dramatically reduced, demonstrating that the plasmonic hot holes facilitated the oxidation of glucose to gluconic acid. In contrast, in the case of L-Au, a moderate decrease in adsorption energy was observed in the first step, and no significant trend was observed in the second step. These might result from the lower substrate specificity of D-glu for L-Au compared to D-Au, as described in Supplementary Fig. S6. These findings emphasized that the adsorption of D-glu on D-Au was much more stable than on L-Au at each oxidation step, promoting the hole-mediated glucose oxidation reaction to form  $\text{H}_2\text{O}_2$  and an acidic environment by producing gluconic acid. To further demonstrate the enantioselective GOD-like reaction of our enzyme-like chiral plasmonic nanoparticles, isothermal titration calorimetry (ITC) was conducted at  $25^\circ\text{C}$ . ITC measurement clarified the thermodynamic profile of the binding and dissociation behavior between D-glu substrates and both D- and L-Au catalysts<sup>27,43</sup> (Fig. 2e–h). The thermogram was obtained by mixing the D-glu substrates solution with D- or L-Au, respectively, as displayed in Fig. 2e, g. Exothermic responses were observed for both D- and L-Au, suggesting that the binding between D-glu and D-/L-Au generates heat. Based on raw ITC thermogram, the integrated heat as a function of molar ratio of D-glu to D-Au or L-Au was obtained and fitted with a simple one-site binding model to investigate the thermodynamic profiles and determine the dissociation constant ( $K_d$ ) (Fig. 2f, h). The dissociation constant of D-glu with D-Au was  $28.2 \mu\text{M}$ , while it was found to be  $60.9 \mu\text{M}$  in the L-Au and D-glu system. These results suggested that the binding affinity between D-Au and D-glu was 2 times higher than that of L-Au and D-glu system, emphasizing the enantioselective GOD-like reaction was more facilitated on the D-Au surface than L-Au. These findings were

consistent with the above DFT calculation results (Supplementary Fig. S6). In addition, thermodynamic profiles were obtained from fitting data, and the difference of Gibbs free energy ( $\Delta G = \Delta H - T\Delta S$ ,  $T = 278 \text{ K}$ ) was calculated.  $\Delta G$  during the binding of D-glu on D-Au was  $-6.3 \pm 0.3 \text{ kcal mol}^{-1}$  ( $\Delta H = -7.039 \pm 0.33 \text{ kcal mol}^{-1}$ ;  $\Delta S = -2.78 \text{ cal mol}^{-1}\text{deg}^{-1}$ ), whereas  $-6.0 \pm 0.5 \text{ kcal mol}^{-1}$  ( $\Delta H = -8.802 \pm 0.57 \text{ kcal mol}^{-1}$ ;  $\Delta S = -10.2 \text{ cal mol}^{-1}\text{deg}^{-1}$ ) was obtained for the binding of D-glu on L-Au surface. These results indicated that the binding process of D-glu on the D-Au surface was slightly more favorable than on the L-Au surfaces. Taken together, enantioselective substrate specificity and chiroptical-dependent hot carrier generation were likely to promote the enzymatic reactions of both D-Au mediated GOD-like and L-AuPd mediated POD-like activities.

### Light-dependent GOD- and POD-like enzymatic performance

Inspired by the mechanism study of our system, enzymatic performance under the CPL was then investigated, as illustrated in Fig. 3. To conduct the CPL-dependent GOD- and POD-like enzymatic performance, we manually set up the light source by integrating a linear polarizer and quarter wave plate with an 808 nm laser, as shown in Supplementary Fig. S7. Under the RC illumination, D-glu selectively interacted with D-Au, which was oxidized to generate gluconic acid by injecting hot holes. In contrast, the hot electrons were injected into  $\text{O}_2$ , leading to the generation of  $\text{H}_2\text{O}_2$ . Subsequently, L-Au generated the hot electrons under LC illumination, which were feasibly concentrated at the Pd active site to facilitate the effective decomposition of  $\text{H}_2\text{O}_2$  to produce the cytotoxic  $\bullet\text{OH}$ , while the remaining hot holes at the Au site participate in the oxidation of  $\text{H}_2\text{O}$  to generate further the cytotoxic  $\bullet\text{OH}$  (Fig. 3a, b and Supplementary Fig. S8). Before evaluating catalytic performance, we monitored the stability of nanoparticles in the acetate buffer (pH 4.5) by measuring DLS, zeta-potential, and SEM images (Supplementary Fig. S9). These results supported that the nanoparticles were well dispersed in the acidic condition without forming aggregation to validate the POD-like activities of L-AuPd further. To





**Fig. 3 | Enzymatic performance under circularly polarized light and linearly polarized light.** **a** Schematic illustration of D-Au and L-AuPd cascade enzymatic reaction under RC and LC. **b** Energy level diagram illustrating the hot charge carrier mediated-catalytic reaction and their reaction pathway.  $E_{\text{vacuum}}$  represents vacuum energy scale and  $E_{\text{NHE}}$  represents electrochemical energy scale relative to a normal hydrogen electrode. (Fermi level of Au and Pd is 5.3 eV and 5.6 eV, redox potential of  $(\text{O}_2/\text{H}_2\text{O}_2) = 0.68 \text{ V}$  and  $(\text{H}_2\text{O}_2/\text{H}_2\text{O}) = 1.77 \text{ V}$ )<sup>36,51</sup>. **c** UV-vis absorption spectra of ox-TMB upon adding L-AuPd and  $\text{H}_2\text{O}_2$  in acetate buffer (pH 4.5) under RC, LC, and L irradiation, demonstrating CPL-dependent catalytic activity with the highest

intensity under LC. DW (deionized water) was used for the control group. **d** Photoluminescence spectra of resorufin upon adding D-Au and glucose under RC, LC, and L irradiation, showing CPL-dependent catalytic activity with the highest intensity under RC. DW (deionized water) was used for the control group. **e** Photoluminescence spectra of terephthalic acid (TA) solution under different NPs and light irradiation conditions. **f** Electron paramagnetic resonance (EPR) spectra of DMPO•OH adducts generated under different NPs and light irradiation conditions. Source data are provided as a Source Data file.

assess the chiroptical-dependent POD-like activity of L-AuPd, the colorimetric assay was performed using 3,3',5,5'-tetramethylbenzidine (TMB) as substrate, and the absorbance at 650 nm was then monitored<sup>44,45</sup>. Colorless TMB was oxidized by •OH to form a blue-colored diamine/diimine charge-transfer complex (ox-TMB), which appeared absorbance at 650 nm. L-AuPd exhibited POD-like activity even without light; however, its catalytic activity improved under light illumination, as confirmed by higher absorbance compared to both neat L-AuPd and L-AuPd +  $\text{H}_2\text{O}_2$  (Fig. 3c and Supplementary Fig. S10a).

Interestingly, L-AuPd under the LC exhibited the most significant absorption peak compared to the linear light (L) and RC, indicating the chiroptical-dependent POD-like activities (Fig. 3c). To evaluate the underlying reaction mechanism of L-AuPd, time-dependent ox-TMB absorption change profiles were monitored with various  $\text{H}_2\text{O}_2$  concentrations (0–80 mM) under LC, L, and RC irradiation. From these profiles, the Michaelis–Menten kinetic model and Lineweaver–Burk model of L-AuPd were obtained (Supplementary Fig. S11 and Supplementary Table S1). Based on the Lineweaver–Burk model, the Michaelis–Menten constant ( $K_m$ ) of L-AuPd was calculated to be 60.083 mM, 67.557 mM, and 51.412 mM for RC, L, and LC irradiation, respectively<sup>46</sup>. Meanwhile, the maximum reaction velocity ( $V_{\text{max}}$ ) values of L-AuPd under RC, L, and LC illumination were obtained at 5.865, 7.775, and  $10.539 \times 10^{-8} \text{ M s}^{-1}$ , respectively, for  $\text{H}_2\text{O}_2$  (Supplementary Table S1). The  $K_m$  value for the  $\text{H}_2\text{O}_2$  substrate under LC irradiation was significantly reduced compared to L or RC, suggesting that the substrate's binding affinity was increased in a chiroptical-dependent manner. The  $V_{\text{max}}$  value of L-AuPd under LC irradiation was the highest compared to RC or L. These results demonstrated that the fast decomposition of  $\text{H}_2\text{O}_2$  occurred at the L-AuPd active site under LC irradiation, further emphasizing the chiroptical-dependent enhancement of POD-like activity.

Next, the chiroptical-dependent GOD-like activity of D-Au was verified. During the glucose oxidation reaction,  $\text{O}_2$  obtains 2 electrons from the Au catalyst to produce the  $\text{H}_2\text{O}_2$ , while the glucose is oxidized to gluconic acid to form an acidic environment that facilitates the POD-like activity of L-AuPd. Firstly, the production of  $\text{H}_2\text{O}_2$  was confirmed

by colorimetric Amplex red assay under light illumination. Amplex red is a representative indicator for validating GOD-like activity, converted to red fluorescent resorufin (peaks at 584 nm) in the presence of  $\text{H}_2\text{O}_2$  and horseradish peroxidase (HRP)<sup>47</sup>. To optimize the substrate concentration, the fluorescence intensity of Amplex red was monitored with various concentrations of D-glu (0.01–1 M). As the D-glu concentration increased, the fluorescence intensity gradually increased (Supplementary Fig. S12). As shown in Fig. 3d and Supplementary Fig. S10b, the D-Au + D-glu case exhibited a slight fluorescence peak at 580 nm compared to the control group (deionized water, D-Au, and D-glu solution), suggesting a moderate GOD-mimic activity of D-Au. Meanwhile, improved fluorescence intensity was observed in the cases of D-Au + D-glu under light illumination. Importantly, the most significant fluorescence intensity was monitored in the case of D-Au + D-glu + RC (red line) compared to the L (green line) or LC (blue line), demonstrating the effective generation of  $\text{H}_2\text{O}_2$  from D-glu at D-Au active site in a chiroptical-dependent manner (Fig. 3d). To further verify whether substrate selectivity varies based on chirality, we conducted the Amplex red assay using both matched and non-matched handedness of Au catalyst and glucose, respectively (Supplementary Fig. S13a–e). The cases of D-Au + D-glu (Supplementary Fig. S13a) and L-Au + L-glu (Supplementary Fig. S13d) showed significantly enhanced fluorescence signals compared to the control group (deionized water), while negligible fluorescence signals were observed in the cases of D-Au + L-glu (Supplementary Fig. S13c) and L-Au + D-glu (Supplementary Fig. S13b) compared to the control group, which were consistent with DFT calculations and ICT measurements. These findings further emphasized that integrating chirality with enzyme-like nanoparticles could significantly improve substrate selectivity. Also, light irradiation resulted in a further increase in fluorescence intensity compared to control groups in all cases. This suggests that the plasmon-mediated hot charge carriers promote the overall glucose oxidation reaction for generating  $\text{H}_2\text{O}_2$  (Supplementary Fig. S13a–d). Then, gluconic acid production was monitored by measuring the pH under light irradiation in a time-dependent manner, as shown in

(Supplementary Fig. S14). The pH of solutions gradually decreased with increasing reaction time in all cases, indicating the effective generation of gluconic acid by D-Au and D-glu under light irradiation. Notably, the decrease in pH was the greatest under the RC illumination, followed by moderate decrease in L, and the least significant decrease in LC. These results originated from the chiroptical-dependent GOD-like performance, which is consistent with previous demonstrations.

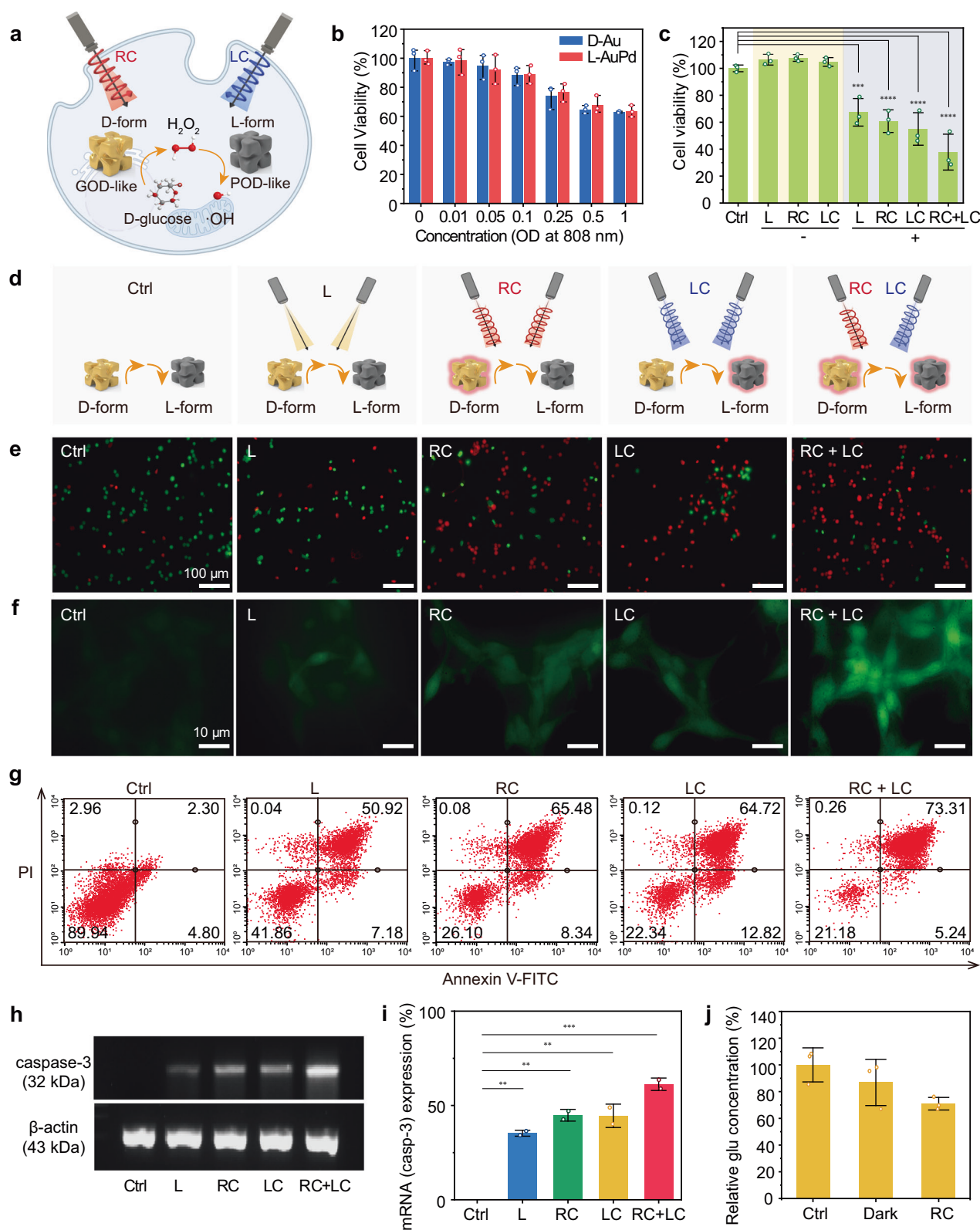
Based on the catalytic performance of both D-Au and L-AuPd, we then assessed the cascade enzymatic properties of our enzyme-like chiral plasmonic nanoparticle system under the RC and LC illumination (Fig. 3e, f and Supplementary Fig. S10c). Terephthalic acid (TA) was used to determine the efficiency of  $\bullet$ OH generation from D-glu through a series of enzymatic reactions. Non-fluorescent TA reacts with  $\bullet$ OH, inducing its transformation into fluorescent hydroxyl-TA with 425 nm emission when excited at 315 nm<sup>48</sup>. Without D-Au and L-AuPd catalysts, negligible peaks at 425 nm were observed (Fig. 3e, dark gray line), indicating that the TA solution remains stable under light irradiation. No peak was observed without D-glu, implying that the cascade enzymatic activity occurred only in the presence of D-glu substrate. (Supplementary Fig. S10c, light gray). D-Au + L-AuPd without light illumination showed a moderate FL peak compared to the illumination conditions, suggesting light illumination effectively enhanced the catalytic performance for both D-Au and L-AuPd (Supplementary Fig. S10c, green line). Also, negligible fluorescence peaks were detected in D-Au (Fig. 3e, f, purple line) and L-AuPd (Fig. 3e, f, blue line) in the presence of D-glu under RC + LC illuminations, suggesting that the presence of both catalysts was mandatory for generating  $\bullet$ OH from D-glu. D-glu incubated with both D-Au and L-AuPd under sole RC or LC irradiation showcased the moderate fluorescence signal compared to under both RC + LC illumination, indicating the  $\bullet$ OH generated effectively through the sequentially activated enzymatic reaction. Importantly, D-Au + L-AuPd under RC + LC illumination showcased the 1.3-fold enhanced fluorescence signal compared to the D-Au + L-AuPd under RC or LC illumination, demonstrating the catalytic efficiency could be improved by manipulating the CPL. These results further supported the chiroptical-dependent properties of our enzyme-like chiral plasmonic nanoparticles, facilitating the  $\bullet$ OH generation using D-glu as a substrate molecule for the cascade enzymatic reaction. Electron paramagnetic resonance (EPR) measurements were then carried out to corroborate further the effective generation of  $\bullet$ OH in various control groups, as shown in Fig. 3f. 5,5-dimethyl-1-pyrroline-N-oxide (DMPO) molecules were used as spin-trapping agents<sup>49</sup>. After spin trapping of  $\bullet$ OH using DMPO, the characteristic EPR signals of DMPO/ $\bullet$ OH adduct appeared with 1:2:2:1 of intensity ratio. D-Au + L-AuPd + RC or D-Au + L-AuPd + LC presented characteristic EPR peaks of DMPO/ $\bullet$ OH adducts with moderate intensity, while D-Au + L-AuPd + RC + LC exhibited the most intense EPR signals. These results further emphasized the effective generation of  $\bullet$ OH in the presence of our enzyme-like chiral plasmonic nanoparticles under both LC and RC illumination.

The above series of experiments persistently verify the excellent ROS-generating properties of our enzyme-like chiral plasmonic nanoparticles through the sequential chiroptical-dependent generation of hot charge carriers. This facilitates the oxidation of D-glu with strong substrate selectivity to produce H<sub>2</sub>O<sub>2</sub>, followed by the reduction of H<sub>2</sub>O<sub>2</sub> at the L-AuPd active site to generate  $\bullet$ OH.

### In vitro cascade enzymatic activities of enzyme-like chiral plasmonic nanoparticles by CPL

Based on the effectiveness of our enzyme-like chiral plasmonic nanoparticles, we then evaluated the therapeutic properties of our system in vitro. To enhance the biocompatibility and dispersity of our nanoparticles, we introduced polyethylene glycol conjugated with the thiol group (PEG-SH) via Au-thiol and Pd-thiol interactions. No morphological changes were observed after conjugating with PEG-SH to both

D-Au and L-AuPd, as depicted in Supplementary Fig. S15. The average size distribution of all samples (D-Au, D-Au@PEG, L-Au, L-AuPd, and L-AuPd@PEG) was measured by dynamic light scattering (DLS). It was approximately 100 nm, suggesting their characteristics were preserved after introducing PEG (Supplementary Fig. S16). We then carried out fourier transform infrared spectroscopy (FT-IR) measurements to further confirm the conjugation of PEG (Supplementary Fig. S17). FT-IR spectra of pure PEG and L-Au@PEG showed the characteristic peak at 1100 cm<sup>-1</sup>, corresponding to C-O stretching in PEG, demonstrating the successful incorporation of PEG-SH into the enzyme-like chiral plasmonic nanoparticles. We then monitor the catalytic effect of D-Au@PEG and L-AuPd@PEG by conducting TMB and Amplex red assay. As shown in Supplementary Fig. S18, the overall catalytic activity of both D-Au and L-AuPd after PEGylation was well preserved, suggesting surface modification did not reduce the overall therapeutic efficacy of our nanoparticles both in vitro and in vivo. In vitro therapeutic properties mediated by cascade GOD- and POD-like activities of our enzyme-like chiral plasmonic nanoparticles were evaluated with colon cancer cells (CT26 and HT29) (Fig. 4a and Supplementary Fig. S19a). Firstly, the dark cytotoxicity of D-Au and L-AuPd was assessed by water-soluble tetrazolium salts (WST-8) assays for various concentrations (optical density at 808 nm: 0–1) (Fig. 4b and Supplementary Fig. S19b). CT26 cells and HT29 cells were incubated with D-Au and L-AuPd for 24 h, respectively, following the absorbance at 450 nm was measured after incubated with WST-8 solution for 30 min. With increasing the concentration of both D-Au and L-AuPd, cell viability gradually decreased but remained insufficient due to the weak generation of  $\bullet$ OH without light illumination. To optimize the light irradiation time, we conducted the time-dependent cell viability test under various irradiation times for CT26 and HT29 cells (Supplementary Fig. S20). RC and LC were irradiated sequentially for equal duration. For both CT26 and HT29, cell viabilities were above ~90% with 5 min of light illumination, suggesting the phototoxicity was negligible. Thus, we proceeded with subsequent experiments under 5 min of light illumination. To assess the light-induced cytotoxicity and demonstrate the CPL-dependent catalytic therapeutic effects in our system, we conducted WST-8 assays under both LC and RC illumination. The samples (OD at 808 nm = 0.1 of D-Au and L-AuPd with ~90% cell viability for CT26 and OD at 808 nm = 0.25 of D-Au and L-AuPd with ~90% cell viability for HT29) were incubated with CT26 and HT29 cells for 24 h under various irradiation conditions (ctrl, L, RC, LC, and RC + LC) as depicted in Fig. 4d and Supplementary Fig. S19d. No phototoxicity was observed without samples under light illumination of L, RC, and LC (Fig. 4c and Supplementary Fig. S19c, light yellow region). However, cells treated with samples exposed to L showed approximately 70% and 80% cell viability for CT26 and HT29, respectively, whereas the most significant cell cytotoxicity (approximately 40% and 60% cell viability for CT26 and HT29, respectively) was observed under both RC + LC illumination (Fig. 4c and Supplementary Fig. S19c, light blue region). Irradiation with RC or LC alone resulted in moderate cell cytotoxicity, falling between the levels observed when only L and RC + LC were irradiated. In the presence of either D-Au or L-AuPd under both RC and LC illumination, the cell survival rates were approximately 70 % and 80 %, respectively. This indicates that when only one of the GOD- or POD-like activities is activated, lower catalytic therapeutic effects are observed compared to when both activities are sequentially activated (Supplementary Fig. S21). These findings demonstrated the chiro-optical-dependent improvement of enzymatic activity in each enzyme-like nanoparticle, leading to an unprecedented decrease in cell viability. Live dead cell assays were conducted using Calcein-AM/PI, further coinciding with the above WST-8 assay results, as shown in Fig. 4e and Supplementary Fig. S19e. To unveil the in vitro ROS generation, 2',7'-dichlorodihydrofluorescein diacetate (DCFH-DA) probe was employed to determine the intracellular ROS levels (Fig. 4f and Supplementary Fig. S19f). The non-fluorescent DCFH-DA reacted



with intracellular ROS within living cells, forming the green-fluorescent 2',7'-dichlorodihydrofluorescein (DCF). Notably, superior fluorescence intensity was disclosed under RC + LC illumination against the other control groups examined (Fig. 4f and Supplementary Fig. S22). Most importantly, these findings emphasized the intended efficiency of our enzyme-like chiral plasmonic nanoparticles and the proposed amplified cascade enzymatic activity, which facilitates catalytic therapeutic effects within the cellular environment. Cell death pathway was then

revealed using flow cytometric analysis (Fig. 4g and Supplementary Fig. S19g). Representatively, the highest occurrence of late apoptosis was observed when cells were incubated with D-Au + L-AuPd under RC + LC illumination (73.3% for CT26 and 53.25% for HT29, respectively) among the evaluated irradiation conditions. In contrast, L, RC, and LC illumination revealed ratios of only 50.9, 65.5, and 64.7% for CT26 and 20.80, 39.72, and 51.88% for HT29, respectively. To further support the apoptotic cell death, we monitored the mRNA expression



**Fig. 4 | In vitro CPL-controlled cascade enzyme reaction for ROS generation.** **a** Schematic diagram of cascade enzymatic reaction of D-Au and L-AuPd under RC and LC in vitro (created in BioRender, <https://Biorender.com/q04a380>). **b** Dark cytotoxicity of CT26 cells with increasing concentrations (optical density at 808 nm) of D-Au and L-AuPd ( $n = 3$  independent experiments). **c** Cell viability of CT26 exposed to CPL without samples (yellow region) and with samples (L-AuPd and D-Au) under different CPL irradiation (blue region) ( $n = 3$  independent experiments). Statistical analysis was conducted by one-way ANOVA test ( $***p < 0.001$ ,  $****p < 0.0001$ ). **d** Schematic illustration of different light irradiation conditions for cascade reaction. The control group was not irradiated. **e** Fluorescence image of Calcein-AM (green)- and PI (red)-contained CT26 cells treated with L-AuPd and D-Au under different CPL irradiation. **f** Fluorescence image of ROS with •OH probe (DCFH-DA) in CT26 cells treated with L-AuPd and D-Au

under different CPL irradiation. **g** Flow cytometry analysis of CT26 cells treated with L-AuPd and D-Au with different CPL irradiation. **h** Agarose gel electrophoresis of RT-PCR amplified Casp-3 mRNA from CT26 cells treated with L-AuPd and D-Au under various CPL conditions.  $\beta$ -actin was used as an internal control. ( $n = 2$  independent experiments). **i** Quantified fluorescent intensity of Casp-3 mRNA staining in gels for each condition. The intensities were normalized to  $\beta$ -actin mRNA expression ( $n = 2$  independent experiments). Statistical analysis was conducted by one-way ANOVA test ( $**p < 0.01$ ,  $***p < 0.001$ ). **j** Relative glucose concentrations in CT26 cells under different conditions ( $n = 3$  independent experiments). Absorbance intensities were normalized to control (untreated and unirradiated). Dark groups were treated with D-Au without irradiation, while RC groups were treated with D-Au and irradiated. Source data are provided as a Source Data file.

level of caspase-3 (Casp-3) through reverse transcription polymerase chain reaction (RT-PCR) (Fig. 4h, i and Supplementary Fig. S19h, i). Agarose gel electrophoresis of RT-PCR-amplified mRNA products and their quantitative analysis revealed the highest Casp-3 expression level in cells treated with D-Au + L-Au Pd under RC + LC illumination. This expression was notably higher when compared to the control groups treated with D-Au + L-AuPd under L, RC, and LC illumination, respectively. These findings strongly support the induction of apoptotic cell death, demonstrating that our system significantly enhances Cas-3 activation, further validating its role in promoting apoptosis in treated cells. We then monitored the cellular GOD-like activity by measuring the glucose level to evaluate the GOD-like activity of D-Au (Fig. 4j, Supplementary Figs. S19j and S23). Both CT26 and HT29 cells treated with D-Au under the RC illumination showed the most significant reduction in cellular glucose levels, while the cells without light illumination showed a moderate reduction, demonstrating the effective GOD-like activity of D-Au under RC irradiation. In summary, the aforementioned results solidify the superior therapeutic effectiveness achieved through the apoptosis pathway.

### In vivo antitumor performance

Inspired by the efficient in vitro anticancer effects, we further assessed the in vivo chiroptical-dependent catalytic cancer treatment using our enzyme-like chiral plasmonic nanoparticles. Samples (OD=1 at 808 nm for D-Au and L-AuPd) were injected intratumorally into CT26 and HT29 tumor-bearing balb/c nude mice. To optimize the duration of light exposure to mice, we monitored the infrared thermography of samples under various exposure times (Supplementary Fig. S24). Photothermal effects of our nanoparticles under the LC, RC, and L were negligible until irradiation reached 10 min. Based on the above thermography results, tumor-bearing mice were exposed to the RC followed by LC for 5 min, respectively (total 10 min irradiation), for subsequent in vivo experiments. The tumor suppression ability was then monitored for 18 days, after which the CT26 and HT29 tumor-bearing mice were sacrificed to measure the corresponding tumor weight and perform histological analysis (Fig. 5a and Supplementary Fig. S26a). Significant tumor suppression was evident exclusively in the light-exposed groups. In contrast, no alterations in tumor growth were exhibited in the group without light (Supplementary Fig. S25a–c). These findings were consistent with the in vitro cytotoxicity assessments (Fig. 4c and Supplementary Fig. S19c). In detail, some inhibition of tumor growth was displayed in L, RC, or LC-treated groups, inferring a moderate ROS generation effect to eradicate the tumor (Fig. 5b and Supplementary Fig. S26b). However, the RC + LC-treated group exhibited the complete elimination of tumor. Promoted generation of ROS could likely induce highly efficient catalytic cancer treatment via chiroptical-activated generation of hot charge carriers. Most importantly, no recurrence was observed in the RC + LC treated group, underscoring the exceptional therapeutic efficacy. The corresponding tumor weight and photographs further supported the aforementioned results (Fig. 5d, Supplementary Figs. S26d, S27 and 28). Throughout

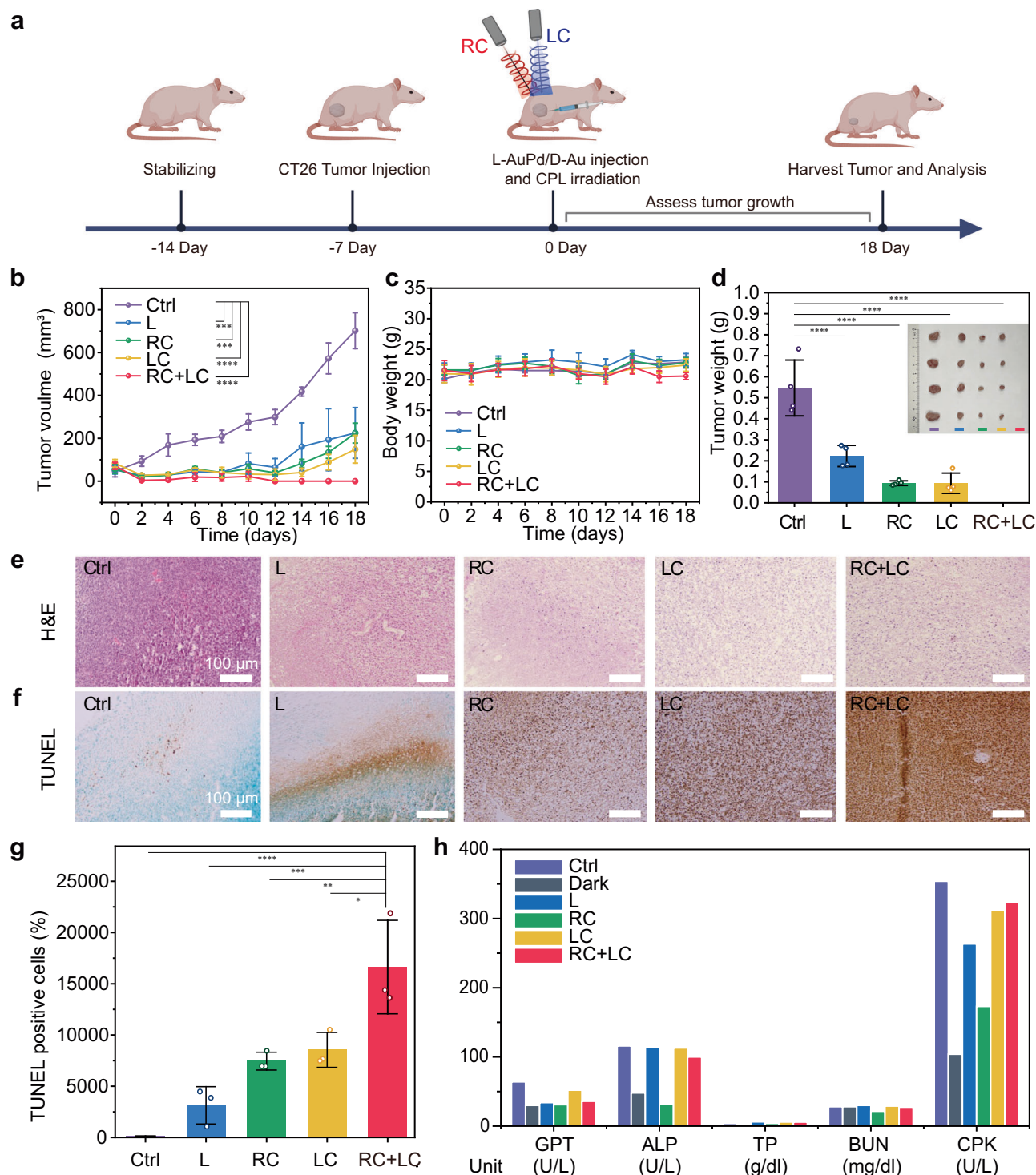
the monitoring period, no changes in body weight were observed, reaffirming the in vivo safety of the PEG-coated chiral plasmonic structures (Fig. 5c, Supplementary Figs. S25d and S26c). We then examined hematoxylin and eosin (H&E)-stained tumor tissue sections to assess the tumor-treating efficacy of our nanoparticles under various light treatment conditions. The RC + LC-treated group exhibited the most severe tumor tissue damage attributed to the enhanced cascade enzymatic activity of D-Au and L-AuPd for catalytic cancer treatment (Fig. 5e and Supplementary Fig. S26e). This observation contrasts sharply with the moderate tumor damage observed in specimens resected from all other irradiation groups (L, RC and LC) and negligible tumor damage was observed in dark condition (Supplementary Fig. S25e, f).

Moreover, we conducted terminal deoxynucleotidyl transferase (TdT)-mediated deoxyuridine triphosphate (dUTP) nick end labeling (TUNEL) staining and the quantitative analysis on tumor sections to ascertain the apoptosis level of tumor cells (Fig. 5f, g). As expected, the highest level of TUNEL-positive signals was exhibited from the RC + LC illuminated group, which aligns well with the H&E staining results for CT26 tumor-bearing mice. In contrast, mice treated with D-Au + L-AuPd under dark condition exhibited no significant TUNEL and Ki67 signals, similar to the control group (Supplementary Fig. S25g–i). For the HT29-bearing mice group, we performed the Ki67 staining and the quantitative analysis on tumor sections to confirm the proliferation level of tumor cells (Supplementary Fig. S26f, g). As expected, the lowest level of Ki67-positive signals was exhibited from the RC + LC illuminated group, demonstrating efficient suppression of tumor proliferation in our system. To investigate the biocompatibility of our nanoparticles, we conducted the additional H&E staining of five major organs (heart, lung, kidney, liver, and spleen) for both CT26 and HT29 tumor-bearing mice. When treated with either PBS or our enzyme-like nanoparticles under RC + LC illumination, there were no signs of abnormal morphological disruption and notable inflammation in major organs, suggesting the biosafety of our enzyme-like nanoparticles (Supplementary Figs. S29 and 30) for both CT26 and HT29 tumor-bearing mice.

Furthermore, the results of blood biochemical analysis, which included measurements of glutamic-pyruvate transaminase (GPT), alkaline phosphatase (ALP), total protein (TP), blood urea nitrogen (BUN), and creatine phosphokinase (CPK), all fell within normal ranges. This indicates minimal systemic toxicity and underscores the biosafety of the PEG-coated chiral plasmonic structures (Fig. 5h and Supplementary Fig. S26h). These results further prove the significant potential of our enzyme-like chiral plasmonic nanoparticles as a CPL-activated catalytic nanomedicine.

In summary, we integrated the chiral plasmonic feature with enzyme-mimicking nanoparticles as a promising CPL-dependent enzyme-like nanoparticle system with highly efficient tumor inhibition ability via adjusting cascade GOD- and POD-like activity. Intrinsic handedness of D-Au enantioselectivity interacted with D-glu substrate, likely natural enzymes, exhibiting a 2-fold stronger binding affinity





**Fig. 5 | In vivo antitumor performance.** **a** Schematic illustration of in vivo experiments with CT26 tumor-bearing mice (created in BioRender, <https://BioRender.com/t51f293>). **b** Tumor suppression profiles of the control group (PBS-treated) and sample treated groups under different light irradiation conditions ( $n = 4$  mice per group). Statistical analysis was conducted by one-way ANOVA test ( $**p < 0.01$ ,  $***p < 0.001$ ). **c** Body weight change profiles of the control group (PBS-treated) and sample treated groups under different light irradiation conditions ( $n = 4$  mice per group). **d** Weight of the dissected tumors of the control group (PBS-treated) and sample treated groups under different light irradiation conditions on day 18. ( $n = 4$  mice per group). Statistical analysis was conducted by one-way ANOVA test ( $****p < 0.0001$ ). Inset: corresponding tumor photograph. scale

bar = 1 cm. Histochemical analyses of **(e)** H&E and **(f)** TUNEL of tumor tissues harvested from control group (PBS-treated) and sample treated groups under different light irradiation. **g** TUNEL positive fluorescence intensity of tumor sections with control group (PBS-treated) and sample treated groups under different light irradiation. ( $n = 3$  independent experiments). Statistical analysis was conducted by one-way ANOVA test ( $*p < 0.1$ ,  $**p < 0.01$ ,  $***p < 0.001$ ,  $****p < 0.0001$ ). **h** Blood biochemical analysis of CT26 tumor-bearing mice after different conditions of CPL irradiation in the presence of D-Au and L-AuPd. The Dark group was not irradiated with CPL in the presence of D-Au and L-AuPd. The control group was treated with PBS. Source data are provided as a Source Data file.

compared to L-Au. Incorporated with plasmonic features, D-Au exhibited significantly enhanced GOD-like activities via LSPR-driven hot charge carriers under the chiral-matched light illumination, i.e., RC. After the irradiation of LC, the POD-like activity of L-AuPd was promoted to decompose the  $\text{H}_2\text{O}_2$  to  $\bullet\text{OH}$  from the D-glu substrate. The overall catalytic performance was enhanced when GOD and POD reactions were sequentially triggered by irradiation with RC followed by LC, demonstrating that chiroptically modulated cascade reactions could lead to effective therapeutic outcomes. Comprehensive in vitro and in vivo experiments have shown that our enzyme-like chiral plasmonic nanoparticles and the underlying strategy achieved successful tumor suppression in the group irradiated with both LC + RC compared to only LC, RC or L irradiated. We believe that our enzyme-like chiral plasmonic nanoparticles, which depend on CPL and enantioselective substrates, create a unique approach to catalytic therapy via cascade reactions.

## Methods

### Ethical regulations

All research complied with the relevant ethical regulations. All animal experiments were conducted based on the relevant laws and institutional guidelines of the Korea Institute of Science and Technology (KIST) and institutional committees (approval number: KIST-2020-073). Male Balb/C nude mice (4–5 weeks) were purchased from Orient Bio Inc. Korea. Animals were stabilized in groups of 4 mice per individual ventilated cage with a 12:12 light-dark cycle and constant room temperature ( $22 \pm 2^\circ\text{C}$ ) and humidity ( $50 \pm 5\%$ ). The maximal tumor size permitted by ethics committee is  $2000\text{ mm}^3$ , and the tumor size in this work was not exceeded.

### Chemicals and reagents

Gold(III) chloride trihydrate ( $\text{HAuCl}_4 \cdot 3\text{H}_2\text{O}$ ;  $\geq 99.9\%$  trace metals basis), Palladium (II) chloride ( $\text{PdCl}_2$ ;  $\geq 99.9\%$ ), L-Ascorbic acid (AA, 99%), L-glutathione (L-GSH, 98%), 3,3',5,5'-Tetramethylbenzidine (TMB,  $\geq 99\%$ ), hexadecyltrimethylammonium bromide (CTAB, 99%), cetyltrimethylammonium chloride solution (CTAC, 25 wt% in  $\text{H}_2\text{O}$ ), terephthalic acid (TA, 98%), 5,5-dimethyl-1-pyrroline n-oxide (DMPO), phosphate-buffered saline tablet (PBS), 2',7'-dichlorodihydrofluorescein diacetate (DCFH-DA,  $\geq 97\%$ ), Annexin V-FITC Apoptosis Detection Kit were purchased from Sigma Aldrich. Hydrogen peroxide ( $\text{H}_2\text{O}_2$ , 35%) was purchased from Daejung chemical.  $\beta$ -D-glucose was purchased from Tokyo chemical industry (TCI). Amplex® Red Hydrogen Peroxide/Peroxidase Assay Kit was purchased from thermofisher scientific. Ez-cytox (Ez-500) was purchased from Dogen bio. Glucose assay kit was purchased from Abcam (ab653333). RNA extraction kit (AccuPrep® Universal RNA Extraction Kit) was purchased from Bioneer ([www.bioneer.co.kr](http://www.bioneer.co.kr)). cDNA synthesis kit (TOPscript™ cDNA Synthesis Kit) was purchased from Enzynomics. The primers (Human qPCR Primer Pair (NM\_004346) and Mouse qPCR Primer Pair (NM\_009810)) used for RT-PCR were purchased from OriGene. All aqueous solutions were prepared using high-purity deionized (DI)-water ( $18.2\text{ M}\Omega\text{ cm}^{-1}$ ).

### Characterization

TEM images and EDS element mapping data were obtained on JEM-2100Plus microscope (JEOL). SEM images were obtained by an energy-dispersive Schottky-field emission scanning electron microscope (JSM-7610). CD spectra were acquired using the JASCO J-1500 CD spectrometer. UV-vis absorption spectra were measured using the Cary 5000 (Varian) spectrometers. X-ray photoelectron spectroscopy (XPS) spectra were recorded by using the Thermo Scientific K-Alpha XPS instrument equipped with a dual-beam source. PL spectra were obtained using FP-8500 (JASCO) spectrometers. ITC experiments were performed using the ITC200 instrument (MicroCal Inc.), and the data were analyzed using the program ORIGIN 7.0 and GraphPad Prism 7.0 software. The Dynamic light scattering (DLS) analysis of the chiral

NPs was conducted by Zetasizer 3000HS analyzer at room temperature. Electron paramagnetic resonance (EPR) measurements were carried out at KBSI western center, using a Bruker EMX/Plus spectrometer. FTIR spectra were measured using the KBr pellet technique on the INVENIO-R spectrometer (Bruker). Cell viability tests were performed using an Infinite M200 PRO microplate reader. All fluorescence images were obtained by using a Nuance FX multispectral imaging system (Cambridge Research & Instrumentation, Inc., USA). The flow cytometry data was obtained by Guava easyCyte flow cytometer. mRNA expressions in the gel were visualized using the iBright FL1500 imaging system (Thermo Fisher).

### Synthesis of chiral gold nanoparticles (L-, D-Au)

The chiral gold nanoparticles were synthesized via peptide-mediated growth method<sup>33,50</sup>. Specifically, the spherical seeds were first synthesized by adding  $\text{NaBH}_4$  (10 mM, 0.8 mL) into a  $\text{HAuCl}_4$  (10 mM, 0.25 mL) containing CTAB (100 mM, 7.5 mL) solution and the solution was kept at  $28^\circ\text{C}$  for 3 h to decompose the remaining  $\text{NaBH}_4$ . Then the octahedral seeds were prepared by growing the spherical seeds in the growth solution, which is composed of 8 mL of water,  $\text{HAuCl}_4$  (10 mM, 0.2 mL), CTAB (100 mM, 1.6 mL), and AA (50 mM, 0.95 mL). After 15 min incubation in  $30^\circ\text{C}$  water bath, the solutions were centrifuged ( $6708 \times g$ , 60 s) and redispersed in 1 mM CTAB solution. Finally, the octahedral seeds were injected in the growth solution prepared by mixing CTAB (100 mM, 0.8 mL),  $\text{HAuCl}_4$  (10 mM, 0.2 mL), AA (100 mM, 0.475 mL) and L-GSH (10 mM, 2.75  $\mu\text{L}$ ), sequentially. After the seeds were added, the reaction solution was left for 2 h at  $30^\circ\text{C}$  water bath without disturbing. The color was changed from transparent to blue with large scattering. Finally, the solution was centrifuged twice ( $1677 \times g$ , 60 s) to eliminate unreacted reagents and was re-dispersed in a 1 mM CTAB solution for further use.

### Synthesis of palladium deposited chiral nanoparticles (L-AuPd)

Synthesized L-Au nanoparticles were re-dispersed in 0.8 mM CTAC, followed by the sequential addition of  $\text{PdCl}_2$  (10 mM, 80  $\mu\text{L}$ ) and ascorbic acid (10 mM, 320  $\mu\text{L}$ ). Then the mixture was allowed to react at  $30^\circ\text{C}$  overnight. After then, the solution was centrifuged twice ( $2775 \times g$ , 60 s) and finally re-dispersed in a 1 mM CTAB solution for further use.

### ITC measurements

The concentration of D-Au in the cell was 100  $\mu\text{M}$ , while the syringe contained 1500  $\mu\text{M}$  of D-glucose or L-glucose. The ITC experiment was carried out using deionized water as a buffer, with titrations conducted at  $25^\circ\text{C}$ . Total of 15 injections of 2  $\mu\text{L}$  each were made at 150 s intervals. The experimental raw data were corrected for dilution by subtracting the values for buffer alone, and then fit by a one-site binding model. Titration data were fitted using a nonlinear least-squares curve-fitting algorithm with three floating variables: stoichiometry (N), binding constant ( $K_d$ ), and change of enthalpy of interaction.

### DFT simulation of enantioselective interaction of D-glu at chiral Au surface

Vienna Ab initio simulation package (VASP) was used to carry out spin-polarized DFT calculations in order to optimize the geometries on the Au(321) surface<sup>20</sup>. To characterize the ionic core, the projector augmented wave (PAW) technique and the Perdew-Burke-Ernzerhof (PBE) generalized gradient functional were used. The van der Waals interaction was taken into consideration using DFT-D3<sup>21</sup>. For the total energy calculations, a  $3 \times 3 \times 1$  Monkhorst-Pack k-point sampling of the Brillouin zone was used in conjunction with a plane wave expansion with a cutoff of 415 eV. The calculations were conducted using the residual minimization method for electronic relaxation and accelerated using Methfessel-Paxton Fermi-level smearing with a width of 0.1 eV. To determine a minimum energy pathway and to compute the

activation barriers, the nudged elastic band method was utilized<sup>22,23</sup>. For Au(321) surface, a 4-layered ( $3 \times 3$ ) surface unit cell with a vacuum spacing of 15 Å was used. For Pd(111) and Au(111) surfaces, ( $2 \times 2$ ) and ( $4 \times 4$ ) surface unit cells were used, respectively, with a 4-layer thickness and a 15 Å vacuum gap.

The adsorption energy,  $E_{ads}$ , is defined as below.

$$E_{ads} = E_{total} - E_{slab} - E_{substrate},$$

where  $E_{total}$  is the total energy of system,  $E_{slab}$  is the energy of bare slab surface,  $E_{substrate}$  is the energy sum of glucose and water molecule in each state. With this definition, a negative adsorption energy corresponds to the energetically favored adsorption on the surface.

### CPL dependent catalytic performance

**TMB experiment for peroxidase-like activity.** The peroxidase-like activity of L-AuPd was assessed by observing the oxidation of 3,3',5,5'-tetramethylbenzidine (TMB) in the presence of  $H_2O_2$  under different CPL irradiation (LC, L, and RC). The L-AuPd nanoparticles (optical density (OD) at 808 nm = 1, 200  $\mu$ l) were suspended in a 2 ml of acetate buffer (0.1 M, pH 4.5) containing TMB and  $H_2O_2$  with the final concentrations of 40 mM for both substrates. The overall reaction was carried out under CPL irradiation (808 nm, 0.9 W cm<sup>-2</sup>) at constant temperature (35 °C). After 30 min reaction, the absorbance of the reactions was measured by UV-vis spectrometer. For the kinetic study of L-AuPd using  $H_2O_2$  as the substrate, concentration of  $H_2O_2$  was varied (0 mM, 10 mM, 20 mM, 40 mM, 60 mM, 80 mM) with fixed concentration of TMB (40 mM). The absorbance changes of ox-TMB at 652 nm ( $\epsilon = 39,000 \text{ M}^{-1} \text{ cm}^{-1}$ ) was recorded with 60 s intervals by UV-vis spectrometer. The kinetic parameters were calculated by fitting the Michaelis-Menten curves and Lineweaver-Burk plot using origin 2024 software. The kinetic data were calculated using the typical Michaelis-Menten equation:  $v = (V_{max} \times [S]) / (K_M + [S])$ , where  $v$  is the initial velocity,  $[S]$  is the concentration of the substrate,  $K_M$  is the Michaelis-Menten constant, and  $V_{max}$  is the maximal reaction velocity.

**Amplex Red Assay for glucose oxidase like activity.** Glucose oxidase like activity of D-Au was evaluated by Amplex® Red Hydrogen Peroxidase Assay Kit according to the provided instruction. D-Au (OD at 808 nm = 1, 200  $\mu$ l) and glucose (0.2 M, 100  $\mu$ l) was added to 1.2 ml of PBS buffer (pH = 7.4). After 30 min reaction under CPL irradiation (808 nm, 0.9 W cm<sup>-2</sup>) at 35 °C, the reaction solution was centrifuged (2775  $\times g$ , 2 min) and 25  $\mu$ l of supernatant was mixed with 950  $\mu$ l deionized water and 25  $\mu$ l of working solution containing Amplex red and HRP. The mixture was incubated in 30 °C oven for 30 min and the fluorescence at 530 nm excitation was measured by the photoluminescence spectroscopy.

**Hydroxyl radical generation efficiency.** Terephthalic acid (TA) was employed to monitor the generation of hydroxyl radicals ( $\cdot OH$ ). A 10 mM TA solution was prepared by dissolving TA in 0.1 M NaOH solution. D-Au (OD at 808 nm = 2, 400  $\mu$ l) and D-glucose (0.2 M, 200  $\mu$ l) were added to 300  $\mu$ l deionized water, and the solution was irradiated with RC for 2.5 min. Immediately after, L-AuPd (OD at 808 nm = 2, 400  $\mu$ l) and prepared TA solution (10 mM, 200  $\mu$ l) were injected to the reaction mixture, followed by irradiation with LC for an additional 2.5 min. After the reaction, the reaction solution was centrifuged (5440  $\times g$ , 60 s) and 1 ml of the supernatant was collected for fluorescence measurement at excitation wavelength of 315 nm. For experiments involving D-Au or L-AuPd under sequential LC and RC irradiation, the same particles were added twice, with the CPL being switched after 2.5 min irradiation period. For experiments with D-Au + L-AuPd with LC or RC, each particle was added to the solution and the same CPL was continuously applied for 5 min.

**EPR measurement.** Electron paramagnetic resonance (EPR) measurements were carried out at KBSI, Seoul, Korea. For the trapping agent, DMPO was used. Before measurement, L-AuPd (OD at 808 nm = 2, 250  $\mu$ l) and D-Au (OD at 808 nm = 2, 250  $\mu$ l) and D-glucose (1 mg/ml, 200  $\mu$ l) were mixed with DMPO solution (10  $\mu$ l). Subsequently, CPL laser (808 nm, 0.9 W cm<sup>-2</sup>) was irradiated for 5 min (LC for 2.5 min and RC for 2.5 min). After reaction, an aliquot of the solution was transferred to a capillary tube (ID: 1.1 mm) and subjected to the EPR measurement. Then the characteristic peaks were detected by EPR spectrometer operating at room temperature. (Frequency: 9.65 GHz, Modulation frequency: 100 KHz, Power 3 mW, Modulation amplitude: 1 G)

### Cell culture

Murine colon cancer cell line (CT-26 (KCLB NO.80009) and HT-29 (KCLB NO.30038)) cells were purchased from the Korean Cell Line Bank. CT26 and HT29 cells were cultured in the medium consisting of Roswell Park Memorial Institute (RPMI) 1640 with the addition of fetal bovine serum (10%) and antibiotic-antimycotic solution (1%) at 37 °C with 5 % CO<sub>2</sub>.

### Cell viability assay

CT26 and HT29 cells were seeded on 96-well plates with a density of  $1 \times 10^4$  cells/well and cultured for 24 h. Cells were washed with Dulbecco's phosphate buffered saline (DPBS) and D-Au@PEG or L-AuPd@PEG were treated with different concentration (OD at 808 nm = 0–1). After samples were incubated for 24 h, the cells were washed with DPBS, following 10  $\mu$ l of WST solution (Ez-cytox) was added and incubated for 30 min at 37 °C. A microplate reader was used to measure the absorbance at 450 nm.

### Cytotoxicity assay

CT26 and HT29 cells were seeded on 96-well plates with a density of  $1 \times 10^4$  cells/well and incubated for 24 h. Then, the cells were washed with DPBS, a mixture of D-Au@PEG and L-AuPd@PEG (OD = 0.1 for CT26 and OD = 0.25 for HT29 at 808 nm, respectively) was added to each well. After 24 h co-incubation, each well was irradiated with different CPL conditions (L, RC, LC, RC + LC) for 5 min. Note that RC + LC groups were irradiated with RC for 2.5 min followed by LC for 2.5 min. For the control group, both samples and light were not treated. For the light irradiated group (yellow box), CPL light was irradiated for 5 min without samples to determine the light toxicity. After light irradiation, the cells were incubated for 24 h. Finally, the cells were washed with DPBS and 10  $\mu$ l of WST solution (Ez-cytox) was added to each well and incubated for 30 min at 37 °C. A microplate reader was used to measure the absorbance at 450 nm.

### Live/Dead cell analysis

CT26 and HT29 cells seeded on confocal glass bottom-dish ( $2 \times 10^5$  cells/dish) were treated with a mixture of D-Au@PEG and L-AuPd@PEG (OD = 0.1 for CT26 and OD = 0.25 for HT29 at 808 nm, respectively). After 24 h incubation, the cells were irradiated with different condition of CPL (L, RC, LC, RC + LC) for 5 min and further incubated for 24 h. For the control group, the light was not irradiated. The cells subsequently washed with DPBS and incubated with calcein-AM (10  $\mu$ g/ml) and PI (20  $\mu$ g/ml) for 15 min. Finally, cells were washed with DPBS and then fluorescence images were obtained by Nuance.

### Evaluation of intracellular ROS generation

CT26 and HT29 cells seeded on confocal dishes ( $2 \times 10^5$  cells/dish) were treated with a mixture of D-Au@PEG and L-AuPd@PEG (OD = 0.1 for CT26 and OD = 0.25 for HT29 at 808 nm, respectively). After 24 h incubation, the cells were washed with DPBS and incubated with DCFH-DA (10 mM) for 30 min. Then, the different condition of CPL light was irradiated (L, RC, LC, RC + LC) for 5 min followed by washing



with DPBS for twice. For the control group, the light was not irradiated. The fluorescence of DCFH-DA was measured by Nuance.

### Cell apoptosis analysis

CT26 and HT29 cells were seeded to 96-well plates with a density of  $1 \times 10^4$  cells/well and cultured for 24 h. Then, cells were treated with a mixture of D-Au@PEG and L-AuPd@PEG (OD = 0.1 for CT26 and OD = 0.25 for HT29 at 808 nm, respectively). After 24 h incubation, the cells were irradiated in different condition of CPL (L, RC, LC, RC + LC) for 5 min and incubated 24 h. For the control group, the light was not irradiated. The cells were subsequently washed with DPBS and incubated with annexin-AM (10  $\mu\text{mol/ml}$ ) and PI (15  $\mu\text{mol/ml}$ ) co-staining solution for 20 min. Finally, cells were collected with a density of  $1 \times 10^5$  cells per group to measure flow cytometry.

### RT-PCR and gel electrophoresis

CT26 and HT29 cells were seeded to 24-well plates with a density of  $5 \times 10^4$  cells/well and cultured for 24 h. Then, cells were treated with a mixture of D-Au@PEG and L-AuPd@PEG (OD = 0.1 for CT26 and OD = 0.25 for HT29 at 808 nm, respectively). After 24 h incubation, the cells were irradiated in different conditions of CPL (L, RC, LC, RC + LC) for 5 min and incubated 24 h. For the control group, the light was not irradiated. The total RNAs were extracted using RNA extraction kit (AccuPrep® Universal RNA Extraction Kit, Bioneer) according to the manufacturer's protocol, and cDNA was synthesized with TOPscript™ cDNA Synthesis Kit (enzymatics). RT-PCR was performed with SYBR Green qPCR PreMIX (enzymatics) and ran on Real-Time PCR (T100 Thermal Cycler, Bio-Rad). The primers used for RT-PCR were purchased from OriGene. (Human qPCR Primer Pair (NM\_004346) and Mouse qPCR Primer Pair (NM\_009810)). The PCR products were electrophoresed on 3% agarose gel.

### Glucose concentration analysis

CT26 and HT29 cells were seeded to 24-well plates with a density of  $5 \times 10^4$  cells/well and cultured for 24 h. The cells were treated with only D-Au@PEG (OD = 0.1 for CT26 and OD = 0.25 for HT29 at 808 nm) for confirming the glucose oxidase like-activity of D-Au. After 24 h incubation, the cells were exposed to RC for 5 minutes, while the dark condition received no irradiation. For the control group, both samples and light were not treated. Following an additional 24 h incubation, glucose concentration was measured using a glucose assay kit (Abcam, ab65333) according to the manufacturer's instructions.

### Measurement of photothermal effect under CPL irradiation

D-Au@PEG and L-AuPd@PEG (OD at 808 nm = 1) particles were each dispersed in 2 ml of deionized water. For the combined sample, equal volumes (1 ml) of D-Au@PEG and L-AuPd@PEG (OD at 808 nm = 1) were mixed. The samples were irradiated using CPL ( $0.9 \text{ W cm}^{-2}$ ) for 10 min. Thermal images of the samples were captured every 2 min by the thermal camera (FLIR Thermo CAM E40). To evaluate the CPL-dependent photothermal effect, the samples were exposed to RC, LC, L light and their temperatures were recorded at 2 min intervals. For the control group, the light was not irradiated.

### Animal experiments

For the preparation of tumor models, 4-5-week-old male Balb/C nude mice were purchased from Orient Bio Inc. Korea. The sex was not considered in this study. The tumor xenografts were established through subcutaneous injection of a suspension of CT26 and HT29 cells ( $1 \times 10^7$  cells in 60  $\mu\text{l}$  of culture medium) into the right flank of the mice. After 2 weeks for preparing, mice were divided randomly into five groups ( $n = 4$ ) and a mixture of D-Au@PEG and L-AuPd@PEG (OD at 808 nm = 5, 50  $\mu\text{l}$ ) was injected into the tumor site by intratumoral injection. Subsequently, each group (L, RC, LC, RC + LC) of the mice were irradiated with CPL laser (808 nm,  $0.9 \text{ W cm}^{-2}$ ) for 10 min. For the

control group, the light was not irradiated. The tumor size (length and width) and body weight were measured every other day. The tumor volume was calculated by the following equation:  $\text{width} \times \text{length} \times \text{height} \times 1/2$ . The mice were sacrificed after 18 days, and the tumor tissues were collected to measure the weight and take photographs.

### Histological analysis

Tumor tissues in each group (Ctrl, L, RC, LC, RC + LC) were collected on 18 days after the treatment and fixed with 4% formaldehyde solution. The sections were stained with hematoxylin and eosin (H&E), Ki67 and terminal deoxynucleotidyl transferase dUTP nick end labeling (TUNEL) for further analysis.

The five major organs (heart, liver, spleen, lung, and kidney) of the control group (PBS treated) and the RC + LC irradiated group were collected on day 18 and fixed with 4% formaldehyde solution for further H&E staining.

Blood samples were collected 18 days after the treatment and centrifuged at 2000 rpm for 5 min to collect plasma and the blood biochemical analysis was performed.

### Statistical and reproducibility

The data here were presented as mean  $\pm$  standard deviation. In the SEM image, microscope and histological analysis experiments, at least three independent experiments were performed, and representative images were shown.

### Reporting summary

Further information on research design is available in the Nature Portfolio Reporting Summary linked to this article.

### Data availability

All data supporting the findings of this study are available within the paper and its Supplementary Information. The full image dataset is available from the corresponding author upon request. Source data are provided with this paper.

### References

- Filice, M. & Palomo, J. M. Cascade reactions catalyzed by bionanostructures. *ACS Catal.* **4**, 1588–1598 (2014).
- Walsh, C. T. & Moore, B. S. Enzymatic cascade reactions in biosynthesis. *Angew. Chem. Int. Ed.* **58**, 6846–6879 (2019).
- Sperl, J. M. & Sieber, V. Multienzyme cascade reactions-status and recent advances. *ACS Catal.* **8**, 2385–2396 (2018).
- Kornecki, J. F. et al. Enzyme production of D-gluconic acid and glucose oxidase: successful tales of cascade reactions. *Catal. Sci. Technol.* **10**, 5740–5771 (2020).
- Wu, H. et al. Development of effective tumor vaccine strategies based on immune response cascade reactions. *Adv. Healthc. Mater.* **10**, 2100299 (2021).
- Hold, C., Billerbeck, S. & Panke, S. Forward design of a complex enzyme cascade reaction. *Nat. Commun.* **7**, 12971 (2016).
- Cao, C. et al.  $\text{Fe}_3\text{O}_4/\text{Ag}/\text{Bi}_2\text{MoO}_6$  photoactivatable nanozyme for self-replenishing and sustainable cascaded nanocatalytic cancer therapy. *Adv. Mater.* **33**, 2106996 (2021).
- Tang, G., He, J., Liu, J., Yan, X. & Fan, K. Nanozyme for tumor therapy: Surface modification matters. *Exploration.* **1**, 75–89 (2021).
- Jana, D. et al. Ultrasmall alloy nanozyme for ultrasound-and near-infrared light-promoted tumor ablation. *ACS Nano* **15**, 7774–7782 (2021).
- Feng, L. et al. An ultrasmall  $\text{SnFe}_2\text{O}_4$  nanozyme with endogenous oxygen generation and glutathione depletion for synergistic cancer therapy. *Adv. Funct. Mater.* **31**, 2006216 (2021).
- Fu, S. et al. Catalytically active  $\text{CoFe}_2\text{O}_4$  nanoflowers for augmented sonodynamic and chemodynamic combination therapy

- with elicitation of robust immune response. *ACS Nano* **15**, 11953–11969 (2021).
12. Chang, M. et al. A multifunctional cascade bioreactor based on hollow-structured  $\text{Cu}_2\text{MoS}_4$  for synergetic cancer chemo-dynamic therapy/starvation therapy/phototherapy/immunotherapy with remarkably enhanced efficacy. *Adv. Mater.* **31**, 1905271 (2019).
  13. Jiang, D. et al. Nanozyme: new horizons for responsive biomedical applications. *Chem. Soc. Rev.* **48**, 3683–3704 (2019).
  14. Hu, X. et al. Biodegradation-mediated enzymatic activity-tunable molybdenum oxide nanourchins for tumor-specific cascade catalytic therapy. *J. Am. Chem. Soc.* **142**, 1636–1644 (2019).
  15. Tian, R. et al. Se-containing MOF coated dual-Fe-atom nanozymes with multi-enzyme cascade activities protect against cerebral ischemic reperfusion injury. *Adv. Funct. Mater.* **32**, 2204025 (2022).
  16. Zhang, Y. et al. Nanozyme decorated metal–organic frameworks for enhanced photodynamic therapy. *ACS Nano* **12**, 651–661 (2018).
  17. Wang, X., Wang, H. & Zhou, S. Progress and perspective on carbon-based nanozymes for peroxidase-like applications. *J. Phys. Chem. Lett.* **12**, 11751–11760 (2021).
  18. Xu, B. et al. Immunomodulation-enhanced nanozyme-based tumor catalytic therapy. *Adv. Mater.* **32**, 2003563 (2020).
  19. Lee, S. H. & Jun, B.-H. Silver nanoparticles: synthesis and application for nanomedicine. *Int. J. Mol. Sci.* **20**, 865 (2019).
  20. Dong, S. et al. Guiding transition metal-doped hollow cerium tandem nanozymes with elaborately regulated multi-enzymatic activities for intensive chemodynamic therapy. *Adv. Mater.* **34**, 2107054 (2022).
  21. Ahmadi, T. S., Wang, Z. L., Green, T. C., Henglein, A. & El-Sayed, M. A. Shape-controlled synthesis of colloidal platinum nanoparticles. *Science* **272**, 1924–1925 (1996).
  22. Wang, Q., Liu, J., He, L., Liu, S. & Yang, P. Nanozyme: a rising star for cancer therapy. *Nanoscale* **15**, 12455–12463 (2023).
  23. Guan, X. et al. Ultrathin 2D Pd/Cu single-atom MOF nanozyme to synergistically overcome chemoresistance for multi-enzyme catalytic cancer therapy. *Adv. Healthc. Mater.* **12**, 2301853 (2023).
  24. Luo, W. et al. Self-catalyzed, self-limiting growth of glucose oxidase-mimicking gold nanoparticles. *ACS Nano* **4**, 7451–7458 (2010).
  25. Mason, S. et al. Biomolecular homochirality. *Chem. Soc. Rev.* **17**, 347–359 (1988).
  26. Cho, N. H. et al. Bioinspired chiral inorganic nanomaterials. *Nat. Rev. Bioeng.* **1**, 88–106 (2023).
  27. Yeom, J. et al. Chiral supraparticles for controllable nanomedicine. *Adv. Mater.* **32**, 1903878 (2020).
  28. Ma, B. & Bianco, A. Regulation of biological processes by intrinsically chiral engineered materials. *Nat. Rev. Mater.* **8**, 1–11 (2023).
  29. Lu, D. et al. Dynamic monitoring of oscillatory enzyme activity of individual live bacteria via nanoplasmonic optical antennas. *Nat. Photonics* **17**, 904–911 (2023).
  30. Liu, C. et al. NIR enhanced peroxidase-like activity of  $\text{Au@CeO}_2$  hybrid nanozyme by plasmon-induced hot electrons and photo-thermal effect for bacteria killing. *Appl. Catal.* **295**, 120317 (2021).
  31. Porath, D., Bezryadin, A., De Vries, S. & Dekker, C. Direct measurement of electrical transport through DNA molecules. *Nature* **403**, 635–638 (2000).
  32. Im, S. W. et al. Chiral surface and geometry of metal nanocrystals. *Adv. Mater.* **32**, 1905758 (2020).
  33. Lee, H.-E. et al. Amino-acid-and peptide-directed synthesis of chiral plasmonic gold nanoparticles. *Nature* **556**, 360–365 (2018).
  34. Negrín-Montecelo, Y. et al. Chiral generation of hot carriers for polarization-sensitive plasmonic photocatalysis. *J. Am. Chem. Soc.* **144**, 1663–1671 (2022).
  35. Probst, P. T. et al. Mechano-tunable chiral metasurfaces via colloidal assembly. *Nat. Mater.* **20**, 1024–1028 (2021).
  36. Gao, W. et al. Electromagnetic induction effect induced high-efficiency hot charge generation and transfer in Pd-tipped Au nanorods to boost plasmon-enhanced formic acid dehydrogenation. *Nano Energy* **80**, 105543 (2021).
  37. Kim, R. M. et al. Enantioselective sensing by collective circular dichroism. *Nature* **612**, 470–476 (2022).
  38. Resasco, J. et al. Enhancing the connection between computation and experiments in electrocatalysis. *Nat. Catal.* **5**, 374–381 (2022).
  39. Lee, J.-E. et al. Plasmon-Enhanced Electrocatalytic Properties of Rationally Designed Hybrid Nanostructures at a Catalytic Interface. *Adv. Mater. Interfaces* **6**, 1801144 (2019).
  40. Chung, K. et al. Electrocatalytic glycerol oxidation enabled by surface plasmon polariton-induced hot carriers in Kretschmann configuration. *Nanoscale* **11**, 23234–23240 (2019).
  41. Fang, G. et al. Differential Pd-nanocrystal facets demonstrate distinct antibacterial activity against Gram-positive and Gram-negative bacteria. *Nat. Commun.* **9**, 129 (2018).
  42. Chen, J. et al. Glucose-oxidase like catalytic mechanism of noble metal nanozymes. *Nat. Commun.* **12**, 3375 (2021).
  43. Hou, K. et al. Chiral gold nanoparticles enantioselectively rescue memory deficits in a mouse model of Alzheimer’s disease. *Nat. Commun.* **11**, 4790 (2020).
  44. Ma, C. B. et al. Guided Synthesis of a Mo/Zn Dual Single-Atom Nanozyme with Synergistic Effect and Peroxidase-like Activity. *Angew. Chem. Int. Ed.* **61**, e202116170 (2022).
  45. Gao, S. et al. Nanocatalytic tumor therapy by biomimetic dual inorganic nanozyme-catalyzed cascade reaction. *Adv. Sci.* **6**, 1801733 (2019).
  46. Wang, Y., Li, T. & Wei, H. Determination of the maximum velocity of a peroxidase-like nanozyme. *Anal. Chem.* **95**, 10105–10109 (2023).
  47. Mishin, V., Gray, J. P., Heck, D. E., Laskin, D. L. & Laskin, J. D. Application of the Amplex red/horseradish peroxidase assay to measure hydrogen peroxide generation by recombinant microsomal enzymes. *Free Radic. Biol. Med.* **48**, 1485–1491 (2010).
  48. Barreto, J. C., Smith, G. S., Strobel, N. H. P., McQuillin, P. A. & Miller, T. A. Terephthalic acid: a dosimeter for the detection of hydroxyl radicals in vitro. *Life Sci.* **56**, 89–96 (1994).
  49. Finkelstein, E., Rosen, G. M. & Rauckman, E. J. Spin trapping of superoxide and hydroxyl radical: practical aspects. *Arch. Biochem. Biophys.* **200**, 1–16 (1980).
  50. Wu, H.-L. et al. A comparative study of gold nanocubes, octahedra, and rhombic dodecahedra as highly sensitive SERS substrates. *Inorg. Chem.* **50**, 8106–8111 (2011).
  51. Sahoo, D. P. et al. Influence of Au/Pd alloy on an amine functionalised ZnCr LDH-MCM-41 nanocomposite: A visible light sensitive photocatalyst towards one-pot imine synthesis. *Catal. Sci. Technol.* **9**, 2493–2513 (2019).

## Acknowledgements

This work was supported by National Research Foundation of Korea (NRF) Grant funded by the Korean Government (2020R1A2C3003958, D.H.K.), by Basic Science Research Program (Priority Research Institute) through the NRF of Korea funded by the Ministry of Education (2021R1A6A1A10039823, D.H.K.), and by the Korea Basic Science Institute (National Research Facilities and Equipment Center) grant funded by the Ministry of Education (2020R1A6C101B194, D.H.K.). This research was supported by the Nano & Material Technology Development Program through the National Research Foundation of Korea (NRF) funded by Ministry of Science and ICT (RS-2024-00409405, K.T.N.). The work at KIST was supported by grants from Korea Institute of Science and Technology (No. 2E33132, S.K.) and the National Research Foundation of Korea (RS-2024-00407093, S.K.).

## Author contributions

All authors revised the manuscript. D.H. Kim conceived the concept and supervised the project. L.P. Lee and K.T. Nam supervised the project. S. Kim supervised the project and provided the experimental facilities. J.W. Han and Y. Kim performed DFT simulation. D.J. Ahn supervised the project and provided experimental facilities on in vivo experiments. H. Kang developed the concrete strategies, conducted the main experiments, analyzed the data, and wrote the manuscript. S. Yu conceived the idea, designed the research and wrote the first draft of manuscript. R.M. Kim synthesized the materials and helped to construct experimental set up. E.E. Kim and S.C. Shin conducted and analyzed the ITC experiments. D. Jang assisted the in vivo experiment. J.H. Han performed FDTD simulation. S.H. Kim and S.K. Hong conducted EPR experiments. All the authors contributed to the preparation of the manuscript.

## Competing interests

The authors declare no competing interests.

## Additional information

**Supplementary information** The online version contains supplementary material available at <https://doi.org/10.1038/s41467-025-57716-7>.

**Correspondence** and requests for materials should be addressed to Jeong Woo Han, Sehoon Kim, Ki Tae Nam, Luke P. Lee or Dong Ha Kim.

**Peer review information** *Nature Communications* thanks Kelong Fan and the other, anonymous, reviewer(s) for their contribution to the peer review of this work. A peer review file is available.

**Reprints and permissions information** is available at <http://www.nature.com/reprints>

**Publisher's note** Springer Nature remains neutral with regard to jurisdictional claims in published maps and institutional affiliations.

**Open Access** This article is licensed under a Creative Commons Attribution-NonCommercial-NoDerivatives 4.0 International License, which permits any non-commercial use, sharing, distribution and reproduction in any medium or format, as long as you give appropriate credit to the original author(s) and the source, provide a link to the Creative Commons licence, and indicate if you modified the licensed material. You do not have permission under this licence to share adapted material derived from this article or parts of it. The images or other third party material in this article are included in the article's Creative Commons licence, unless indicated otherwise in a credit line to the material. If material is not included in the article's Creative Commons licence and your intended use is not permitted by statutory regulation or exceeds the permitted use, you will need to obtain permission directly from the copyright holder. To view a copy of this licence, visit <http://creativecommons.org/licenses/by-nc-nd/4.0/>.

© The Author(s) 2025

<sup>1</sup>Department of Chemistry and Nanoscience, Ewha Womans University, Seoul, Republic of Korea. <sup>2</sup>Harvard Medical School, Harvard University; Department of Medicine, Brigham and Women's Hospital, Boston, MA, USA. <sup>3</sup>Department of Materials Science and Engineering, Seoul National University, Seoul, Republic of Korea. <sup>4</sup>Department of Chemical Engineering, Pohang University of Science and Technology, Pohang, Gyeongbuk, Republic of Korea. <sup>5</sup>Technological Convergence Center, Research Resources Division, Korea Institute of Science and Technology, Seongbuk-gu, Seoul, Republic of Korea. <sup>6</sup>Department of Biomicrosystem Technology, Korea University, Seoul, Republic of Korea. <sup>7</sup>Western Seoul Center, Korea Basic Science Institute, Seoul, Republic of Korea. <sup>8</sup>Biomedical Research Institute, Korea Institute of Science and Technology, Hwarang 14-gil 5, Seongbuk-gu, Seoul, Republic of Korea. <sup>9</sup>Department of Chemistry, Chung-Ang University, Seoul 06974, Republic of Korea. <sup>10</sup>KU-KIST Graduate School of Converging Science and Technology, Korea University, Seoul, Republic of Korea. <sup>11</sup>Chemical and Biological Integrative Research Center, Korea Institute of Science and Technology, 5 Hwarang-ro 14-Gil, Seongbuk-gu, Seoul, Republic of Korea. <sup>12</sup>Department of Bioengineering, University of California, Berkeley, Berkeley, CA, USA. <sup>13</sup>Department of Electrical Engineering and Computer Science, University of California, Berkeley, Berkeley, CA, USA. <sup>14</sup>Department of Biophysics, Institute of Quantum Biophysics, Sungkyunkwan University, Suwon, Republic of Korea. <sup>15</sup>College of Medicine, Ewha Womans University, Gangseo-gu, Seoul, Republic of Korea. <sup>16</sup>Graduate Program in Innovative Biomaterials Convergence, 52 Ewhayeodae-gil, Seodaemun-gu, Ewha Womans University, Seoul, Republic of Korea. <sup>17</sup>Basic Sciences Research Institute (Priority Research Institute), Ewha Womans University, Seoul, Republic of Korea. <sup>18</sup>Nanobio-Energy Materials Center (National Research Facilities and Equipment Center), Ewha Womans University, Seoul, Republic of Korea. <sup>19</sup>These authors contributed equally: Haeun Kang, Subin Yu, Ryeong Myeong Kim. ✉ e-mail: [jwhan98@snu.ac.kr](mailto:jwhan98@snu.ac.kr); [sehoonkim@kist.re.kr](mailto:sehoonkim@kist.re.kr); [nkitae@snu.ac.kr](mailto:nkitae@snu.ac.kr); [lplee@bwh.harvard.edu](mailto:lplee@bwh.harvard.edu); [dhkim@ewha.ac.kr](mailto:dhkim@ewha.ac.kr)